

JET-POWERED SUPERNOVAE OF $\sim 10^5 M_\odot$ POPULATION III STARS ARE OBSERVABLE BY *EUCLID*, *WFIRST*, *WISH*, AND *JWST*

TATSUYA MATSUMOTO¹, DAISUKE NAKAUCHI², KUNIHITO IOKA^{3,4,5} AND TAKASHI NAKAMURA¹

Draft version October 13, 2018

ABSTRACT

Supermassive black holes observed at high redshift $z \gtrsim 6$ could grow from direct collapse black holes (DCBHs) with mass $\sim 10^5 M_\odot$, which result from the collapse of supermassive stars (SMSs). If a relativistic jet is launched from a DCBH, it can break out of the collapsing SMS and produce a gamma-ray burst (GRB). Although most of the GRB jets are off-axis from our line of sight, we show that the energy injected from the jet into a cocoon is huge $\sim 10^{55-56}$ erg, so that the cocoon fireball is observed as ultra-luminous supernovae of $\sim 10^{45-46}$ erg s⁻¹ for $\sim 5000[(1+z)/16]$ days. They are detectable by the future telescopes with near infrared bands, such as, *Euclid*, *WFIRST*, *WISH*, and *JWST* up to $z \sim 20$ and $\lesssim 10$ events per year, providing a direct evidence of the DCBH scenario.

Subject headings: gamma-ray burst: general - supernova - quasars: supermassive black holes - stars: Population III

1. INTRODUCTION

Since the last decade, supermassive black holes (SMBHs) with $\sim 10^9 M_\odot$ have been discovered in the high-redshift quasars (QSOs) at $z \gtrsim 6$ (Fan 2006; Mortlock et al. 2011; Wu et al. 2015). The origin of these SMBHs is one of the biggest riddles in the Universe. We do not know how the seed BHs acquire mass of $\sim 10^9 M_\odot$ within a short time of $\lesssim 1$ Gyr (the age of the Universe at $z \gtrsim 6$).

Plausible candidates for the seeds are stellar mass BHs of $\sim 10^{1-3} M_\odot$, which are the end products of first stars or Population III (Pop III) stars. Theoretical studies have shown that Pop III stars are typically very massive ($\sim 10^{2-3} M_\odot$; Bromm et al. 1999, 2002; Abel et al. 2002; Yoshida et al. 2003, 2006, 2008; Susa et al. 2014; Hirano et al. 2014; Hosokawa et al. 2015). Stellar mass seeds are difficult to grow to be supermassive within $\lesssim 1$ Gyr as long as the mass accretion continues with the Eddington rate. Such continuous and efficient accretion may be prevented by the radiation feedback effects (Milosavljević et al. 2009; Alvarez et al. 2009; Park & Ricotti 2011, 2012, 2013; Aykutaalp et al. 2014). Some authors suggest that supercritical accretion may help the stellar mass BHs to grow rapidly (Volonteri & Rees 2005; Madau et al. 2014; Inayoshi et al. 2015a; Alexander & Natarajan 2014).

A more attractive seed may be provided by the supermassive Pop III stars (SMSs) of $\sim 10^5 M_\odot$. SMSs are formed in primordial gas clouds which are under intense far ultra-violet (FUV) radiations (Omukai 2001; Bromm & Loeb 2003; Dijkstra et al. 2008;

Agarwal et al. 2012; Johnson et al. 2014; Agarwal et al. 2015; Agarwal & Khochfar 2015; Schauer et al. 2015) or in the high density and high temperature regions which are formed through the cold inflow onto a protogalaxy and/or galaxy mergers (Inayoshi & Omukai 2012; Inayoshi et al. 2015b). When SMSs collapse via the general relativistic (GR) instability (Chandrasekhar 1964) or the exhaustion of the nuclear fuel, they leave massive BHs of $\sim 10^5 M_\odot$ as remnants. We call these massive BHs as direct collapse BHs (DCBHs). With the Eddington accretion rate, such massive seeds can grow up to SMBHs of $\sim 10^9 M_\odot$ for ~ 0.5 Gyr. This is shorter than the age of the Universe at $z = 7$, where the most distant QSO is found (Mortlock et al. 2011).

The detection of violent explosions, like supernovae (SNe) and gamma-ray bursts (GRBs), produced by SMSs may be useful to understand their contribution to the SMBH formation (Johnson et al. 2013; Whalen et al. 2013a,b; Chen et al. 2014). In the previous paper, we studied whether SMSs can produce GRBs or not, and discussed their detectability (Matsumoto et al. 2015). GRBs are produced by the relativistic jets which are launched from BH-accretion disk systems. In the collapsar scenario, the BH and disk system are formed in the center of a massive star, when it collapses (Woosley 1993; MacFadyen & Woosley 1999) (see also, Lamb & Reichart 2000; Gou et al. 2004; Mészáros & Rees 2010; Suwa & Ioka 2011; de Souza et al. 2011; Nagakura et al. 2012; Nakauchi et al. 2012; Mesler et al. 2014, for Pop III collapsars). After the relativistic jet breaks out of the progenitor envelope, it can contribute to the γ - and X-ray prompt emission. If the direction of the jet axis coincides with our line of sight, we can observe it as a GRB.

The stellar evolution theory suggests that SMSs have very large radii of 10^{14-15} cm, which are comparable to or even larger than red supergiants (Fryer & Heger 2011; Hosokawa et al. 2012, 2013; Sakurai et al. 2015). Although one may think that the bloated envelope prevents the relativistic jet from breaking out of it success-

¹ Department of Physics, Kyoto University, Kyoto 606-8502, Japan

² Astronomical Institute, Tohoku University, Aoba, Sendai 980-8578, Japan

³ Theory Center, Institute of Particle and Nuclear Studies, KEK, Tsukuba 305-0801, Japan

⁴ Department of Particle and Nuclear Physics, SOKENDAI (The Graduate University for Advanced Studies), Tsukuba 305-0801, Japan

⁵ Yukawa Institute for Theoretical Physics, Kyoto University, Kyoto, 606-8502, Japan

fully, we have found that the breakout is possible because of the steeply-declining density profile. We have also found that the GRBs from SMSs show ultra-long durations of $\delta t_\gamma \sim 10^{4-6}$ s, which are about 10^{3-5} times longer than ordinary GRBs and even longer than the observed ultra-long GRBs (ULGRBs⁶). The isotropically radiated energy of the GRBs amounts to as much as $E_{\gamma, \text{iso}} \sim 10^{56}$ erg, which is also by an order of magnitude larger than that of the most energetic GRB. They could be detectable by the Burst Alert Telescope (BAT) onboard the *Swift* satellite (Barthelmy et al. 2005) up to $z = 20$. Thus, very energetic ULGRBs are a unique feature of the GRBs from SMSs.

However, the prompt emission has some disadvantages. First, the detection rate of such GRBs was estimated to be low $\lesssim 2 (\Psi_{\text{GRB}}/10^{-8} \text{yr}^{-1} \text{Mpc}^{-3})(\theta/5^\circ)^2 \text{yr}^{-1}$ on the whole sky, where Ψ_{GRB} is the intrinsic event rate of the SMS GRBs, and θ is the opening angle of the jet. Second, we cannot measure the distance or redshift only through the high energy emission, because it is difficult to identify the host galaxy. In order to overcome these disadvantages, we consider the counterparts of SMS GRBs which radiate isotropically in the optical or near infrared (NIR) bands.

In the previous study, we find that energy of 10^{55-56} erg is injected into the hot plasma cocoon which surrounds a jet before its breakout (Matsumoto et al. 2015). When the jet propagates in the progenitor envelope, it forms two shock waves at the jet head. One is a forward shock which sweeps the envelope materials, and the other is a reverse shock which decelerates the jet materials. The materials in the jet head can expand sideways and form a hot plasma cocoon around the jet (Matzner 2003). The cocoon can also expand in the envelope and finally breaks out of it along with the jet head. We call the cocoon component emerging out of the progenitor star as a cocoon fireball.

Some authors suggested that the cocoon fireball evolves like an SN ejecta, if the cocoon loads the stellar material efficiently before breakout (Kashiyama et al. 2013; Nakauchi et al. 2013). Nakauchi et al. (2013) showed that the super-luminous SN (SLSN) associated with the ULGRB 111209A can be reproduced by the emission from the cocoon fireball, if the progenitor is a blue supergiant of $\sim 10^{13}$ cm. For SMSs, it takes much longer time for the jet head to break out of the envelope, so that we can expect much larger energy stored in the cocoon and much brighter emission from the cocoon fireball.

In this paper, we study the cocoon emission associated with the ULGRBs from SMSs. We find that they can be observed as ultra-luminous SNe up to $z \sim 20$ by the future NIR surveys. We also show that the distance or redshift of the event can be identified by the Gunn-Peterson trough (Gunn & Peterson 1965). Furthermore, we find how to estimate the mass of the progenitor, its radius, and the explosion energy from the observables, such as the bolometric luminosity, duration, and photospheric velocity. This enables us to confirm that the

⁶ So far, ULGRBs are discovered in the low- z Universe of $z \lesssim 1$ (Gendre et al. 2013; Levan et al. 2014). They have typical durations of $\delta t_\gamma \sim 10^4$ s and the isotropically radiated energy of $\sim 10^{53}$ erg.

Table 1
Parameters of cocoon fireballs

Progenitor Model	1E5	Accreting
E_c [erg]	1.0×10^{56}	4.2×10^{55}
M_c [M_\odot]	1.1×10^3	3.5×10^2
$R_c(0)$ [cm]	1.2×10^{14}	2.8×10^{15}

Notes. The energy E_c , mass M_c , and initial radius $R_c(0)$ of cocoon fireballs are shown. The values of the energy E_c and mass M_c are evaluated at the jet breakout. The cocoon initial radius $R_c(0)$ means the cocoon radius at the start of homologous expansion (see Appendix A and B for the definition of these quantities). The 1E5 model is a SMS which evolves from a metal-free ZAMS star. The Accreting model is a massive protostar growing under rapid-mass accretion of $1 M_\odot \text{yr}^{-1}$ (see the text).

progenitor is a SMS. Finally, we discuss that from the detection rate by the future NIR surveys, we can constrain the conditions and environments for the SMS formation.

We organize this paper as follows. In Section 2, we show the light curves of the cocoon emission and discuss their detectability with future telescopes. In Section 3, we consider the observational strategy for the cocoon emission and their event rate. In Appendix, we collect the formulae for calculating the cocoon parameters and the light curves. Throughout this paper, we consider the Λ CDM cosmology and adopt the cosmological parameters as : $H_0 = 67.8 \text{ km s}^{-1} \text{Mpc}^{-1}$, $\Omega_m = 0.308$ and $\Omega_\Lambda = 0.692$ (Planck Collaboration et al. 2015).

2. ULTRA-LUMINOUS SNE FROM SUPERMASSIVE COLLAPSARS

In this section, first we briefly explain the SMS formation and our progenitor models. Next, we show the light curves of the cocoon emission comparing with other SN events. Then, we show the light curves for the future telescopes and discuss the detectability.

While hydrogen molecules are the main coolant in a primordial gas cloud, they can be destroyed via photodissociation or collisional dissociation when the cloud is irradiated with the intense FUV field or is in a highly shock-compressed region. Such a gas cloud can contract by its self-gravity only via hydrogen atomic cooling, so that the temperature of the cloud is kept high ($\sim 10^4$ K). A protostar formed in the center of the contracting cloud accretes the surrounding gas with a high accretion rate of $\dot{M} \sim 0.1 - 1 M_\odot \text{yr}^{-1}$. If the accretion can continue over the stellar lifetime $\sim \text{Myr}$, the protostar can become a SMS of $\sim 10^5 M_\odot$ (see also, Wise et al. 2008; Regan & Haehnelt 2009a,b; Shang et al. 2010; Wolcott-Green et al. 2011; Latif et al. 2013; Schleicher et al. 2013; Regan et al. 2014; Inayoshi & Haiman 2014; Becerra et al. 2015).

We consider two models of SMSs in this work (for more details of our models, see Matsumoto et al. 2015). First, if the accretion is halted by e.g., radiation feedback when the star obtains $\sim 10^5 M_\odot$, the SMS reaches the zero age main sequence (ZAMS). Fryer & Heger (2011) calculated the evolution of a SMS of $10^5 M_\odot$ from the ZAMS stage until it exhausts its nuclear fuels and begins to collapse. We use the density profile at the precollapse phase as a progenitor model, and call it as the ‘‘1E5 model’’. Second, if the accretion continues without any interruption, they grow up to the critical mass where the GR instability sets in (Chandrasekhar 1964). Then the ac-

creting SMS will become unstable and finally collapse. Hosokawa et al. (2013) calculated the evolution of an accreting SMS with the constant and high accretion rate of $\dot{M} = 1 M_{\odot} \text{ yr}^{-1}$. They stopped the calculation when the star obtains $10^5 M_{\odot}$, since they suffered from some numerical difficulties. While the GR instability has not set in yet, we adopt the density profile of this phase as a progenitor model, and call it as the “Accreting model”. As long as the accretion continues, the envelope profile will not change so much and it should have little effect on our results.

It should be noted that our progenitor models are calculated without taking rotation into account. In reality, GRB progenitors are thought to be rotating for the jet formation. When the progenitors are rotating very rapidly, the stellar structure may also become chemically homogeneous (Yoon & Langer 2005; Woosley & Heger 2006). This may change the radii of the progenitors. However, as long as the progenitor envelopes are radiation-pressure-dominated and have steeply-decreasing density profiles, the jet heads do not decelerate and can penetrate the stellar surface (see Appendix A, for the jet propagation in a radiation-pressure-dominated envelope).

First, we calculate the dynamics of a relativistic jet in a progenitor envelope, and figure out the total energy E_c and mass M_c loaded on a cocoon. We show the details of our model in Appendix A, along with the order of magnitude estimates. In Table 1, we show the results of the energy E_c , mass M_c at the jet breakout, and initial radius $R_c(0)$ of the cocoon fireballs when homologous expansion starts (see also Appendix B). The quantities E_c and M_c can be roughly reproduced by the analytical estimates (Eqs. A10 and A15). We find that the energy of the cocoon fireball is very large $E_c \sim 10^{55-56}$ erg. This is because the progenitors have a very large radius. It takes much time for the jet head to break out of the progenitor envelope, so that a large amount energy is stored in the cocoon. This can be seen from Eqs. (A9) and (A10). We can see that the cocoon fireballs are non-relativistic, $E_c \ll M_c c^2$, and initially optically thick, $\tau_0 \sim \kappa M_c / R_c(0)^2 \gg 1$, where c is the speed of light and $\kappa = 0.35 \text{ cm}^2 \text{ g}^{-1}$ is the Thomson scattering opacity for the primordial composition. Thus, the cocoon fireball may evolve like a shock heated ejecta of Type IIP SNe (Kashiyama et al. 2013; Nakauchi et al. 2013).

Next, using the parameter values in Table 1, we calculate the light curves of the cocoon emission. We show the details of our prescription in Appendix B. In Fig. 1, we compare the light curves of the cocoon emission obtained from the 1E5 and Accreting model with those of the observed SNe. The horizontal axis shows the time from the peak of the light curve (for the cocoon emission, we represent the time in the progenitor frame). The vertical axis gives the absolute magnitude in the R-band. The red and green solid curves correspond to the 1E5 model and the Accreting model, respectively. We see that the cocoon emission are about 10 – 100 times brighter than even SLSNe. Its bolometric luminosity amounts to $10^{45-46} \text{ erg s}^{-1}$ (Eq. B7), so that we call them as ultra-luminous SNe. Such ultra-luminous SNe may be useful to study the early Universe.

From the green solid line in Fig. 1 (the Accreting

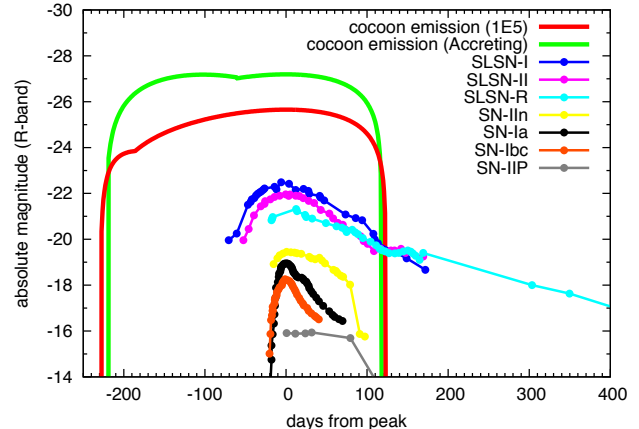


Figure 1. Light curves of cocoon emission and other observed SNe. The horizontal axis shows days from their peaks in the light curves (For the cocoon emission, we represent the time in the progenitor frame). The vertical axis represents the absolute magnitude in the R-band. The red and green curves are the light curves of the cocoon emission for the 1E5 and Accreting models, respectively. The blue, magenta, light-blue, yellow, black, orange, and grey curves show the light curves of observed transient events, Type-I super-luminous SN (SLSN-I) PTF09cnd, Type-II SLSN SN2006gy, Type-R SLSN SN2007bi, Type IIn SN 2005cl, Type Ia SN, Type Ibc SN, and Type IIP SN 1999em, respectively. These light curves are taken from Fig. 1 in Gal-Yam (2012).

SMS model), we find that the light curve can be divided into two parts, and that each part has its own peak. They come from the different thermal states in the cocoon fireball (Appendix B). Around the first peak the ejecta has very high temperature, so that the atoms are completely ionized. In this phase, the effective temperature decreases with time according to Eq. (B8), so that the spectral peak moves to the redder bands with time. When the effective temperature drops below the critical value ($T_{\text{ion}} \sim 6000 \text{ K}$), the atoms recombine in the ejecta. In the recombined ejecta, photons can escape almost freely, so that the recombination front becomes the photosphere. Since the recombination front moves inwards to the expanding ejecta, the photospheric radius looks almost unchanged in the lab-frame observer (Eq. B14). Then, the spectral energy distribution hardly changes with time, and the light curve shows a plateau. This phase corresponds to the plateau phase in Type I IP SNe. The light curves of the cocoon emission drop abruptly at ~ 120 days from the peaks. This is because the photosphere reaches the center of the cocoon fireball and all photons diffuse out from the ejecta.

Finally, we discuss the detectability of the cocoon emission with the future wide-field NIR survey telescopes, such as *Euclid* (Laureijs et al. 2011), *WFIRST* (Spergel et al. 2013), and *WISH*⁷ (see also section 3). We show the property of each telescope in Table 2. We set the redshifts of the events as $z = 10, 15,$ and 20 , where SMSs are suggested to be formed (Agarwal et al. 2012; Dijkstra et al. 2014; Yue et al. 2014). At these redshifts, intergalactic hydrogen will be still neutral (Planck Collaboration et al. 2015), so that the emission with wavelengths shorter than $\lambda_{\text{obs}} = 0.122(1+z) \mu\text{m}$ is strongly absorbed. Therefore, we can use only red-

⁷ <http://www.wishmission.org/en/index.html>

Table 2
Properties of future NIR telescopes

Telescope	<i>Euclid</i>	<i>WFIRST</i>	<i>WISH</i>
Band	Y,J,H	Y,J,H,F184	1-4.5 μm
Depth(SN survey) [mag]	26	29.3-29.4(J,H ^a)	—
Area(SN survey) [deg ²]	40	5.04	—
Duration(SN survey) [yr]	3	0.5	—
Cadence [day]	4-6	5	—
Depth(galaxy survey) [mag]	24	26.2-26.9	28
Area(galaxy survey) [deg ²]	1.5-2.0 $\times 10^4$	2.0 $\times 10^3$	100
Duration(galaxy survey) [yr]	3	1.3	5

Notes. Area in line 4 and 8 means the size of the observed region by each telescopes. In SN survey, telescopes observe the same regions many times and detect transient events. In galaxy survey, telescopes survey large areas just once and observe galaxies.

^a *WFIRST* is planned to have three types of SN surveys (Spergel et al. 2013). In this paper, we only consider the SN deep survey, because it has the best sensitivity. The SN deep survey uses only J- and H-bands.

Table 3
Center wavelength and maximum redshift of each band

Band name	Y	J	H	F184	K	L
wavelength [μm]	1.020	1.215	1.654	1.842	2.179	3.547
z_{max}	7.4	9.0	12.6	14.2	18.6	28.2

Notes. In line 2, we show the center wavelength of each band. At the maximum redshift of z_{max} in line 3, the center wavelength is equal to the redshifted Lyman- α wavelength, $\lambda_{\text{Band}} = \lambda_{\text{Ly}\alpha}(1 + z_{\text{max}})$.

der bands than the redshifted Lyman- α wavelength. In Table 3, we show, for each band, the maximum redshift up to which photons at the band center are free from Lyman- α absorption.

In Figs. 2 - 5, we show the light curves of the cocoon emission for the 1E5 SMS model, and compare them with the detection limit of *Euclid*, *WFIRST*, and *WISH*, respectively. The horizontal axis represents the time since the cocoon fireballs start homologous expansion in the observer frame. The vertical axis shows the observed AB magnitude. *Euclid* has a difficulty to detect the cocoon emission in galaxy survey because the cocoon emission is not bright enough. In the SN survey, *Euclid* can detect the first peak of the cocoon emission for ~ 80 days. *WFIRST* can detect only the first peak of the cocoon emission at $z = 10$. In the galaxy survey, the first peak can be observed for ~ 90 and 120 days in H- and F184-bands, respectively, while in the SN survey, it can be observed for ~ 300 days. It should be noted that *WFIRST* uses only J- and H-bands in the SN survey (see Table 2). At $z = 15$, photons at the F184-band are strongly absorbed, so that the cocoon emission cannot be detected with *WFIRST*. *WISH* has the deeper detection limits and more bands than those of *Euclid* and *WFIRST* in the galaxy survey. At $z = 10$, *WISH* can detect the first peak in all bands with durations of longer than 100 days. In L-band, *WISH* will observe the whole of the light curves with the duration of ~ 3800 days. In K-band, the first and second peak are detected separately. At $z = 15$, *WISH* will detect the first peak in K- and L-bands. In L-band, the second peak is also detectable. At $z = 20$, only L-band can be used. *WISH* can detect the first peak with the duration of ~ 400 days.

In Figs. 6 - 8, we show the light curves of the cocoon emission obtained from the Accreting SMS model. In the Accreting SMS model, the duration of the first peak is comparable to that of the second one, because the

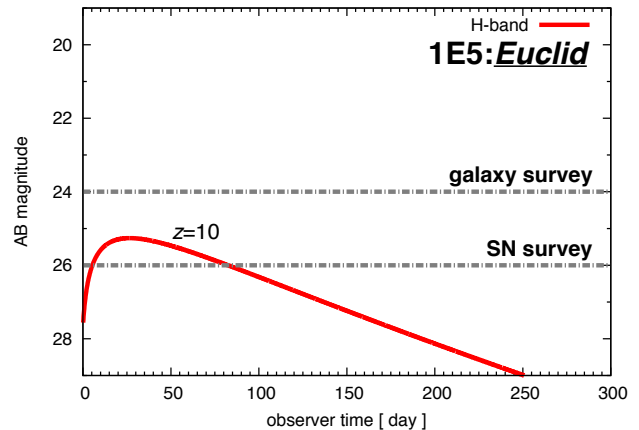


Figure 2. Light curves of cocoon emission for the 1E5 SMSs observed with *Euclid*. The horizontal axis shows the observer time since the cocoon fireball starts homologous expansion. The vertical axis shows the observed AB magnitude. The red curve shows the light curve in H-band. We show the sensitivities of *Euclid*'s SN survey and galaxy survey with horizontal grey dash-dotted lines. *Euclid* can detect only the first peaks of the cocoon emission in the SN survey.

Accreting SMSs have larger radius than the 1E5 SMSs (Eq. B10). The large radius also makes cocoon emission about 10 times brighter than those of the 1E5 SMS model (Eq. B7). *Euclid* can detect the first peak in H-band for more than 600 days. *WFIRST* also detects the first peak in all available bands for $\gtrsim 1000$ days. In the SN survey, it may observe the second peak with the duration of ~ 3000 days in H-band. *WISH* can detect the first peak up to $z = 20$ in all bands for 1000 - 3000 days. In particular, the first and second peaks are observed for $\sim 3700 - 5400$ days in K- ($z = 10$) and L-bands ($z = 10$ and 15), respectively.

3. REDSHIFT DETERMINATION AND EVENT RATE

3.1. Redshift Determination

In the previous section, we find that the cocoon emission from SMSs may become ultra-luminous SNe. They can be detectable with the future wide-field NIR survey telescopes, such as *Euclid*, *WFIRST*, and *WISH*. In this section, we discuss the survey strategy of these ultra-luminous SNe.

The NIR survey telescopes have two survey modes, the

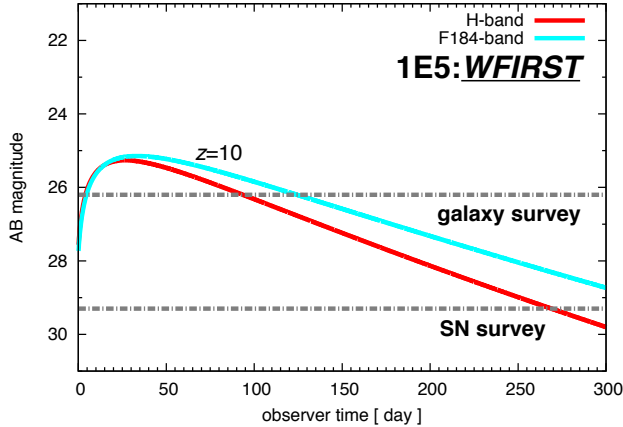


Figure 3. Same as Fig. 2, but for the $1E5$ SMSs observed with *WFIRST*. We add the light curves in F184-band with a light-blue curve. *WFIRST* can observe only the first peaks of the cocoon emission at $z = 10$ for more than 90 days. It should be noted that in SN survey, *WFIRST* uses only J- and H-bands.

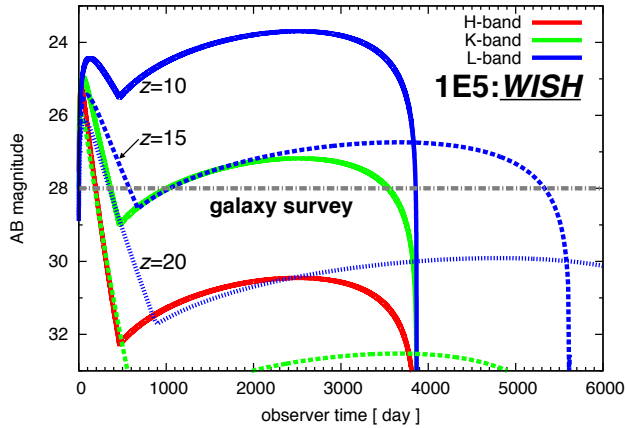


Figure 4. Same as Fig. 2, but for the $1E5$ SMSs observed with *WISH*. We add the light curves in K- and L-bands with green and blue curves. The solid, dashed and dotted curves correspond to the redshifts of the progenitors $z = 10, 15,$ and $20,$ respectively. Before the recombination sets in ($t_{\text{obs}} \lesssim 500$ days), the light curves show the bright first peaks. After $t_{\text{obs}} \gtrsim 500$ days, they show the second peaks.

SN and galaxy surveys. In the SN survey, they visit the same area many times. By comparing the images taken at different times, they can detect cocoon emissions as transient events. As shown in Table 2, in the SN survey, the telescopes cover much narrower areas than those in the galaxy survey. This will reduce the number of detectable events (see the next section). However, the telescopes observe more deeply than they do in the galaxy survey. The sensitive observation with high cadence in the SN survey will enable us to detect the cocoon emissions without confusing with other events.

In the galaxy survey, they survey large areas and take images of many galaxies. They can detect cocoon emissions as one of the brightest stationary sources at high redshift. Since the survey area in the galaxy survey is larger than that in the SN survey, we can expect larger event rate in this mode. A color-color diagram is use-

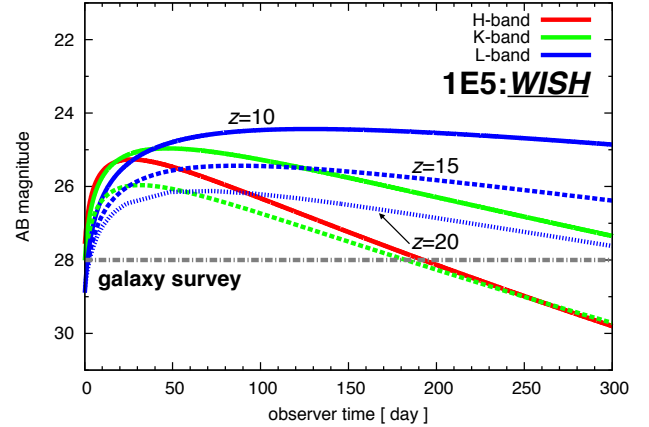


Figure 5. Same as Fig. 4, but we zoom in on the first 300 days (rising first peak).

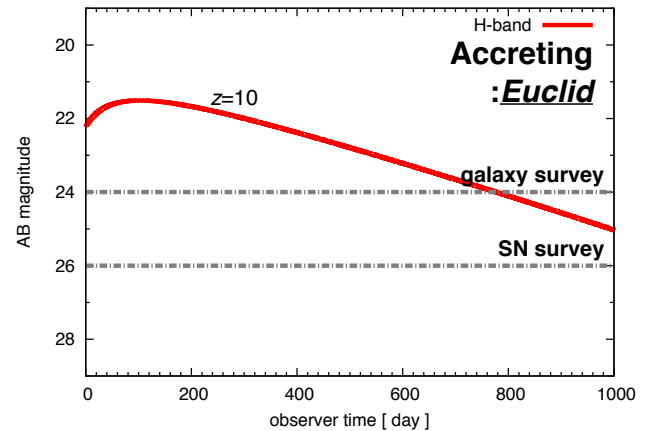


Figure 6. Same as Fig. 2, but for the Accreting SMS model.

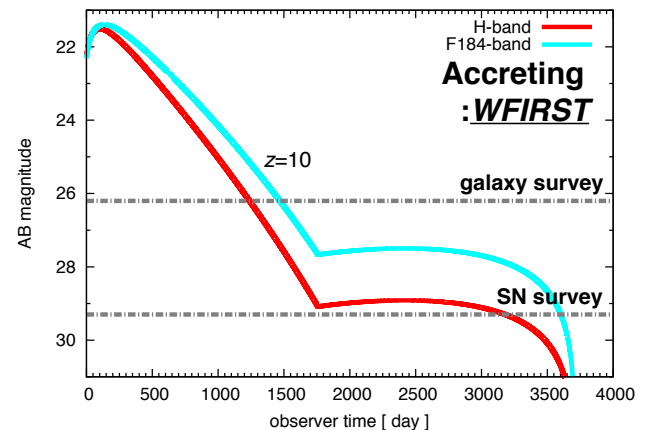


Figure 7. Same as Fig. 3, but for the Accreting SMS model.

ful to discriminate the cocoon emission from other objects such as QSOs or brown dwarves (Mesinger et al. 2006; Tanaka et al. 2013). Because of Lyman- α absorption in short wavelengths, we can select the candidates of the cocoon emission as red objects in a color-color

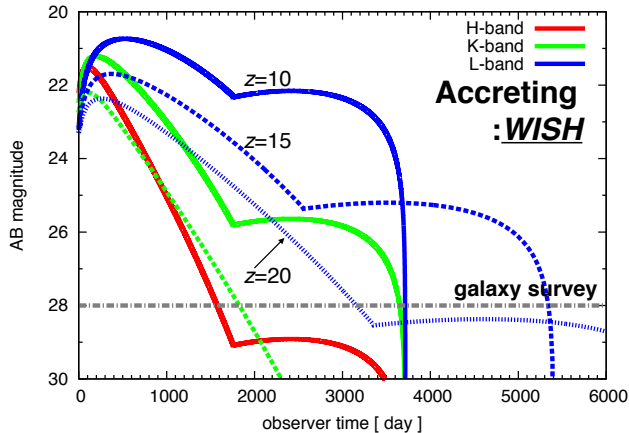


Figure 8. Same as Fig. 4, but for the Accreting SMS model.

diagram. It should be noted that the cocoon emission is one of the brightest sources at high redshift, making it easy to disentangle the cocoon emissions from high- z galaxies. We estimate the luminosity of the cocoon emissions in Eq. (B7) as $L_{\text{cocoon}} \sim 10^{45} \text{ erg s}^{-1}$, which is about 100 times larger than that of ordinary galaxies $L_{\text{gal}} \sim 10^{10} L_{\odot}$. We do not have the luminosity functions of galaxies at $z \gtrsim 10$, but we know the luminosity function at $z \sim 8$ obtained by BoRG survey as $\phi(L) = \phi_*(L/L_*)^\alpha \exp[-L/L_*]$, where $\phi_* \simeq 4 \times 10^{-4} \text{ Mpc}^{-3}$, $\alpha \simeq -2$, and $L_* \simeq 1.1 \times 10^{10} L_{\odot}$ (Bradley et al. 2012). By assuming that this function holds at $z \gtrsim 8$, we estimate the number density of the galaxies, whose luminosity is comparable with that of the cocoon emissions, as $\sim 10^{-8} \text{ Gpc}^{-3}$. Therefore, the possibility that we detect bright galaxies as the cocoon emissions is extremely low (see the next section for the event rate of the cocoon emissions). We can also use the time variability of cocoon emissions to disentangle cocoon emissions from galaxies. Follow-up observations will find that the color of cocoon emissions becomes redder than that at the first detection (see below).

In Fig. 9, we show the temporal evolution of the spectral energy distribution (SED) of the cocoon emission at $z = 10$. It is obtained from the Accreting SMS model. The horizontal axis corresponds to the wavelength in the observer frame. The vertical axis represents the observed flux density. The dark-grey shaded region shows the wavelength region in which photons are absorbed by neutral hydrogen in the intergalactic medium (IGM). The light-grey shaded regions correspond to the J-, H-, K-, and L-bands from left to right, respectively. The horizontal dashed lines represent the best sensitivities of *Euclid*, *WFIRST*, and *WISH*. We also show the sensitivities of *James Webb Space Telescope (JWST)* (Gardner et al. 2006), in the spectroscopic and photometric observations with the dash-dotted and dotted curves, respectively. *JWST* is useful for the follow-up spectroscopy.

From Fig. 9, we find that the flux is above the detection limit of *JWST* spectroscopy for $t_{\text{obs}} \lesssim 1000$ days. In this case, we can identify the absorption edge of the SED, which is made by Lyman- α absorption. Then, the distance or redshift of the event may be measured spectroscopically by the Gunn-Peterson trough, as is often

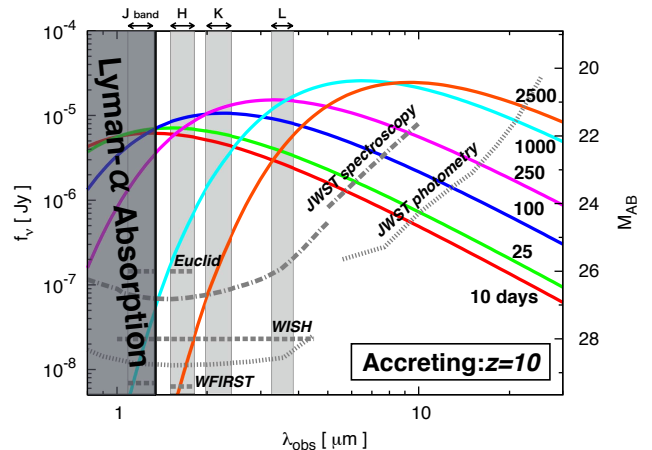


Figure 9. Time evolution of the spectral energy distribution (SED) of the cocoon emission from the Accreting SMS at $z = 10$. The horizontal axis shows the wavelength in the observer frame. The vertical axis represents the flux density. The SEDs after 10, 25, 100, 250, 1000, and 2500 days are shown with the red, green, blue, magenta, light-blue, and orange solid curves, respectively. We represent the wavelength range in which photons suffer from Lyman- α absorption with dark-shaded region. We also show the regions which correspond to J-, H-, K- and L-bands with light-shaded regions. The grey dashed lines in J-, H-, K-, and L-bands represent the best sensitivities of *Euclid*, *WFIRST*, and *WISH*. The grey dash-dotted and dotted curves also show the sensitivities of *JWST* in the spectroscopic and photometric observations^a, respectively. The Lyman- α damping at $\lambda_{\text{obs}} \lesssim 1.34[(1+z)/11] \mu\text{m}$ tells us the redshift of the burst.

^a<http://www.stsci.edu/jwst/science/sensitivity>

done in the QSO observations (Gunn & Peterson 1965).

We can obtain the spectroscopic information around the first peak of the cocoon emission for $t_{\text{obs}} \lesssim 2500$ days. If the SED can be taken around of the first peak, we can estimate the bolometric luminosity at the first peak $L_{1\text{st}}$. As shown in Eq. (B7), the bolometric luminosity decreases monotonically, and we use Eq. (B7) at $t = 0$ for the luminosity $L_{1\text{st}}$ below. The decreasing rate of the bolometric luminosity gives the diffusion time of the cocoon fireball in the observer frame $t_d(1+z)$. We will also be able to estimate the photospheric velocity v_{ph} from e.g., the P Cygni profile of the hydrogen Balmer line ($\lambda_{\text{H}\alpha} = 0.656(1+z)\mu\text{m}$). It should be noted that around the first peak, the photospheric velocity v_{ph} is evaluated by the cocoon velocity v_c (Eq. B9). The observables in the first peak are useful to estimate the progenitor's parameters, because the first peak is brighter in band ranges of the *Euclid*, *WFIRST*, and *WISH* photometry and the *JWST* spectroscopy.

From Eqs. (B5), (B7), and (B9), the energy E_c , mass M_c , and initial radius R_c of the cocoon fireball can be obtained as functions of the observables, $L_{1\text{st}}$, t_d , and

v_{ph} , as

$$M_c = \frac{4\pi c}{3\kappa} t_d^2 v_{\text{ph}} \quad (1)$$

$$\simeq 1.8 \times 10^3 M_\odot t_{d,7}^2 v_{\text{ph},10},$$

$$E_c = \frac{4\pi c}{5\kappa} t_d^2 v_{\text{ph}}^3 \quad (2)$$

$$\simeq 2.2 \times 10^{55} \text{ erg } t_{d,7}^2 v_{\text{ph},10}^3,$$

$$R_c = \frac{5\kappa}{2\pi c} L_{1\text{st}} v_{\text{ph}}^{-2} \quad (3)$$

$$\simeq 9.3 \times 10^{13} \text{ cm } L_{1\text{st},45} v_{\text{ph},10}^{-2},$$

where $t_{d,7} = t_d/10^7 \text{ s}$, $L_{1\text{st},45} = L_{1\text{st}}/10^{45} \text{ erg s}^{-1}$, and $v_{\text{ph},10} = v_{\text{ph}}/10^{10} \text{ cm s}^{-1}$.

When the bolometric luminosity does not change so much around the first peak, we can use the total duration of the cocoon emission Δt_{co} in order to estimate the diffusion time t_d . This situation actually occurs when the recombination starts at much faster than the diffusion timescale. From Eqs. (3), (B10), and (B18), we obtain the diffusion timescale as

$$t_d = \frac{(4\pi\sigma_{\text{SB}}T_{\text{ion}}^4)^{1/5}}{7^{1/2}} L_{1\text{st}}^{-1/5} v_{\text{ph}}^{2/5} \Delta t_{\text{co}}^{7/5} \quad (4)$$

$$\simeq 5.9 \times 10^6 \text{ s } L_{1\text{st},45}^{-1/5} v_{\text{ph},10}^{2/5} \Delta t_{\text{co},7}^{7/5},$$

where σ_{SB} is the Stefan-Boltzmann constant and $\Delta t_{\text{co},7} = \Delta t_{\text{co}}/10^7 \text{ s}$. We can substitute this expression for t_d in Eqs. (1) and (2).

Litvinova & Nadezhin (1985) and Popov (1993) also gave the expressions for the parameters of Type IIP SNe progenitors, by using the duration, luminosity, and photospheric velocity in the plateau phase (i.e., the second peak). Their expressions have been used to derive the explosion parameters of Type IIP SNe (Hamuy 2003; Bose et al. 2013; Dhungana et al. 2015). When we use the observables of the second peak, i.e., the bolometric luminosity $L_{2\text{nd}}$ and the photospheric velocity $v_{\text{ph}}(t_{2\text{nd}})$, rather than $L_{1\text{st}}$ and v_{ph} , Eqs. (B18), (B20), and (B21) become dependent and we cannot solve for the parameters M_c , E_c , and $R_c(0)$. This is not pointed out in the previous studies (Litvinova & Nadezhin 1985; Popov 1993), in which they use $v_c = (5E_c/3M_c)^{1/2}$ rather than $v_{\text{ph}}(t_{2\text{nd}})$, but we think that $v_{\text{ph}}(t_{2\text{nd}})$ (not v_c) is the observable quantity for the second peak.

From Eq. (A15), the progenitor mass can be estimated by using Eq. (1)

$$M_* \sim 6.4 \times 10^4 M_\odot t_{d,7}^2 v_{\text{ph},10} \times \left(\frac{\eta_{\text{h}}}{6.2 \times 10^{-4}} \right)^{1/2} \left(\frac{\theta}{5^\circ} \right)^{-2}, \quad (5)$$

If this is larger than the theoretical mass of any Pop III stars via hydrogen molecular cooling (Hirano et al. 2014), the observation gives the first direct evidence of a SMS.

The spectroscopic observation also tells us the existence of metals in the cocoon fireballs (see also, Wang et al. 2012, for probing the metal enrichment in the early IGM with GRB afterglows). With taking the ratio of line strengths, we can infer the abundance of

heavy elements. If SMSs are really made of the primordial gas and the cocoon fireballs are metal free, we will observe only hydrogen and helium lines. This is a direct evidence of Pop III stars. Thus, the cocoon emission from SMSs provides us an unique opportunity to explore the Pop III SMSs.

3.2. Event Rate

Here, we discuss the event rate of the cocoon emission. The cumulative number of cocoon emission events observed with a telescope with a survey area Ω_{obs} is calculated by

$$\Delta N(z) = \int_0^z \Psi_{\text{burst}}(z') 4\pi cr(z')^2 \left| \frac{dt}{dz} \right| dz' \Delta t_{\text{obs}} \frac{\Omega_{\text{obs}}}{4\pi}, \quad (6)$$

where $\Psi_{\text{burst}}(z)$, $r(z)$ and Δt_{obs} are the intrinsic burst rate in the comoving volume, the comoving distance, and the observation time, respectively. The intrinsic event rate $\Psi_{\text{burst}}(z)$ is related to the SMS or DCBH formation rates ($\frac{dn_{\text{SMS}}}{dt}$ or $\frac{dn_{\text{DCBH}}}{dt}$), which are studied in previous studies. In the following rate estimation, we simply assume that the SMS GRB event rate Ψ_{burst} is proportional to the SMS formation rate $\frac{dn_{\text{SMS}}}{dt}$ as, $\Psi_{\text{burst}} = f_{\text{GRB}} \frac{dn_{\text{SMS}}}{dt}$, where f_{GRB} is a fraction of the GRB formation. It should be noted that since the cocoon emission emits photons isotropically, the event rate is not suppressed by the jet beaming factor $\sim \theta^2$ like GRBs.

The formation theories of SMSs or DCBHs have a lot of unknown parameters, e.g. the star formation efficiency, the escape fraction of FUV photons from the host halo, the metal enrichment via galactic outflow, and the reionization history of the Universe. We should determine which model predicts a correct formation rate by observations.

In Fig. 10, we show the SMS GRB rates converted from the SMS formation rates, as $\Psi_{\text{burst}} = f_{\text{GRB}} \frac{dn_{\text{SMS}}}{dt}$. The vertical axis shows the SMS GRB rate in comoving volume per redshift. Pink, light-blue, and orange shaded regions show the SMS GRB rates given by the SMS formation rates which are calculated by Agarwal et al. (2012), Dijkstra et al. (2014), and Yue et al. (2014)⁸, respectively. Since there are no constraints on the conversion parameter f_{GRB} , we also consider four cases of the parameter values of $f_{\text{GRB}} = 1, 0.1, 0.01, \text{ and } 0.001$ and plot each case separately. The case of $f_{\text{GRB}} = 1$ means that all SMSs produce ULGRBs and cocoon emissions. This will be an upper limit of the SMS GRB rate and the true GRB rate will be lower than that. In the local Universe, the GRB rate is about 10^{-3} times of the core-collapse SN rate (Wanderman & Piran 2010). The local fraction corresponds to $f_{\text{GRB}} = 0.001$.

We also show the formation rates which give event rates = 1 event yr^{-1} per redshift by the observations with *Euclid*, *WFIRST*, and *WISH*, using red, green, and blue curves, respectively. The solid and dashed curves represent the galaxy and SN survey modes, respectively. These rates are obtained by equating the integrand in

⁸ Dijkstra et al. (2014) and Yue et al. (2014) show only the cumulative number densities of DCBHs. Then, we convert their results into the formation rates.

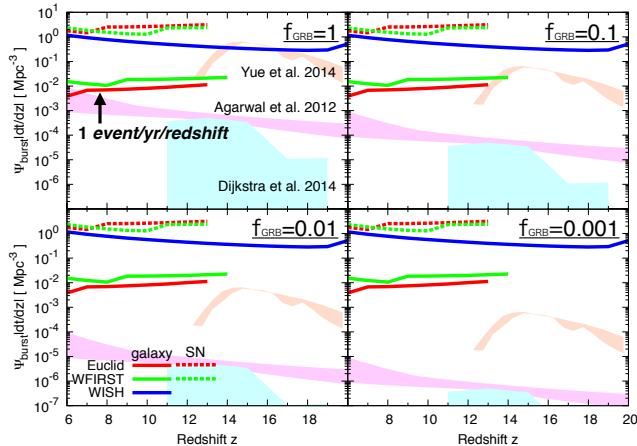


Figure 10. SMS GRB event rates in comoving density per redshift converted from the SMS formation rates as $\Psi_{\text{burst}} = f_{\text{GRB}} \frac{dn_{\text{SMS}}}{dz}$. The pink, light-blue, and orange shaded regions represent the GRB rates given by the SMS formation rates which are calculated by Agarwal et al. (2012), Dijkstra et al. (2014) and Yue et al. (2014), respectively. The upper-left, -right, bottom-left, and -right panels show the cases of the GRB fraction $f_{\text{GRB}} = 1, 0.1, 0.01,$ and $0.001,$ respectively. The red, blue, and green curves show the formation rates which give 1 event yr^{-1} per redshift by observation with future telescopes *Euclid*, *WFIRST*, and *WISH*, respectively. The solid and dashed curves represent the galaxy and SN survey modes, respectively.

Eq. (6) as unity. Since the probability of detections increases when the duration of events Δt_{co} is longer than the observation time Δt_{obs} , we multiply Eq. (6) by the modifying factor $\Delta t_{\text{co}}/\Delta t_{\text{obs}}$.

If a model predicts more formation rate than the rates represented by solid or dashed curves in Fig. 10, we expect that we observe the cocoon emission more than 1 event yr^{-1} . From Fig. 10, we see that the

models studied by Yue et al. (2014) predict much more event rate than those studied by Agarwal et al. (2012) and Dijkstra et al. (2014). Actually, the cumulative event rate reaches $\sim 30 (f_{\text{GRB}}/1)$ events yr^{-1} for the model studied by Yue et al. (2014). On the other hand, Agarwal et al. (2012) and Dijkstra et al. (2014)'s models predict $\lesssim 1 (f_{\text{GRB}}/1)$ event yr^{-1} .⁹ Thus, by the actual observations with the future telescopes, we can select preferred models.

For its 11 yrs of operation, BAT onboard *Swift* satellite has never detected ULGRBs from SMSs. However, this result gives little constraint on the SMS GRB event rate nor DCBH formation rate. The detectability of SMS GRBs with BAT depends on the models of a progenitor star and the prompt emission (Matsumoto et al. 2015). Then, for some models, BAT does not have enough sensitivity to detect the GRBs. On the other hand, the cocoon emissions are detectable with all future telescopes, and their simple emission mechanism gives few uncertainties to the detectability. We can discuss the DCBH formation rate, which is essentially unconstrained, more robustly using the cocoon emission than using the SMS GRB.

ACKNOWLEDGMENTS

We thank K. Inayoshi, K. Kashiyama, K. Sugimura, and H. Yajima for fruitful discussion. We also thank for A. Heger for giving us his numerical data which were used in the previous paper, which was written with him, and the present paper. This work is supported in part by the Grant-in-Aid from the Ministry of Education, Culture, Sports, Science and Technology (MEXT) of Japan, Nos. 261051 (DN) 24103006, 26287051, 24000004, 26247042 (KI) 24103006, 15H02087 (TN).

APPENDIX

A. ANALYTICAL ESTIMATE FOR COCOON PARAMETERS

It is very useful to develop analytical formulae for cocoon parameters in order to see the dependences on progenitors' properties. We estimate the cocoon energy E_c and mass M_c at the jet breakout analytically in this appendix. For more details of our jet propagation model, see Matsumoto et al. (2015).

First, we calculate the cocoon energy E_c at the jet breakout defined as the energy stored into a cocoon component during the jet propagation in a progenitor as

$$E_c = \eta_c \int_{t_{\text{in}}}^{t_{\text{b}}} L_j dt, \quad (\text{A1})$$

where η_c , t_{in} , t_{b} and L_j are the fraction of matter flowing into the cocoon from the jet head, the jet injection time, the jet breakout time, and the jet luminosity, respectively. It should be noted that we set the origin of time when the progenitor starts to collapse. We evaluate the efficiency parameter η_c as unity because the jet head is sub relativistic in the progenitor. In the following, we estimate the quantities t_{in} , t_{b} , and L_j .

Let us first estimate the jet luminosity L_j . In our study, we consider the MHD mechanism as the jet formation process (Blandford & Znajek 1977). In this mechanism, the jet luminosity L_j is given by the mass accretion rate onto the central BH as $L_j = \eta_j \dot{M} c^2$ (Komissarov & Barkov 2010), where the efficiency parameter $\eta_j = 6.2 \times 10^{-4}$ is calibrated to reproduce observed total energy of a jet when we apply our jet propagation prescription to Wolf-Rayet stars (Suwa & Ioka 2011). We assume that a mass shell at mass coordinate $M_r = \int_0^r 4\pi r^2 \rho dr$ falls onto the BH in

⁹ The formation rate of DCBHs depends strongly on the critical intensity of the FUV field which is needed for the SMS formation. Agarwal et al. (2012) and Dijkstra et al. (2014) calculated the formation rate by adopting $J_{\text{crit}} = 30 - 300$, where J_{crit} is the intensity at $h\nu = 12.4 \text{ eV}$ and in units of $10^{-21} \text{ erg s}^{-1} \text{ cm}^{-2} \text{ Hz}^{-1} \text{ sr}^{-1}$.

Recently, Sugimura et al. (2014) obtained $J_{\text{crit}} \simeq 1000$ by considering the realistic spectra of the FUV field from metal-poor galaxies. This value is larger than those used in Agarwal et al. (2012) and Dijkstra et al. (2014), so that they may overestimate the formation rate to some extent (see also, Inayoshi & Tanaka 2015).

Table 4
Parameters of density profiles

Progenitor Model	1E5	Accreting
$\rho_{\text{core}} [\text{g cm}^{-3}]$	4.6×10^6	2.3
$R_{\text{core}} [\text{cm}]$	1.0×10^{10}	1.0×10^{12}
$R_* [\text{cm}]$	5.8×10^{13}	1.4×10^{15}
$M_{\text{core}} [M_{\odot}]$	9.6×10^3	4.8×10^3

its free-fall time defined as $t_{\text{ff}}(r) = \sqrt{\pi^2 r^3 / 8GM_r}$, where G is the gravitational constant. Then we obtain the mass accretion rate as $\dot{M} = (dM_r/dr)/(dt_{\text{ff}}/dr)$.

While the launching mechanisms of relativistic jets are still uncertain, the following two mechanisms are often discussed: (i) MHD mechanism (Blandford & Znajek 1977) and (ii) neutrino and antineutrino annihilation mechanism (Popham et al. 1999). In the latter model, as the mass of a central BH gets larger, the energy density in the accretion disk becomes smaller, so that the jet could be quenched before the jet breakout (Zalamea & Beloborodov 2011; Suwa & Ioka 2011). On the other hand, in the MHD jet model, the jet luminosity depends only on the mass accretion rate and is proportional to the accretion rate, $L_j \propto \dot{M}$. Therefore, as long as the mass accretion rate onto the central BH is large and there is a global magnetic field, a powerful jet could be sustained regardless of the BH mass nor the energy density around the BH. In our previous paper, we find that in the SMS case, high mass accretion rates ($\dot{M} \gtrsim 0.1 M_{\odot}/\text{s}$) could last for more than 10^4 s, which is longer than the jet breakout time ~ 4000 s (see Fig. 3 in Matsumoto et al. 2015).

We see that once we know the density profile $\rho(r)$, we can calculate the quantities M_r , t_{ff} , and \dot{M} . SMSs have a density profile proportional to r^{-3} at their radiation-pressure-dominated envelope (Matzner & McKee 1999). Then, we approximate the density profile as follows,

$$\rho(r) = \begin{cases} \rho_{\text{core}} & r < R_{\text{core}}, \\ \rho_{\text{core}} \left(\frac{r}{R_{\text{core}}}\right)^{-3} & R_{\text{core}} < r < R_*, \end{cases} \quad (\text{A2})$$

where ρ_{core} and R_{core} are the density and radius of the stellar core, where the density is constant. In Table 4, we show these parameters for our progenitor models (these density profiles are shown in Figs. 1 and 6 in Matsumoto et al. 2015). With this simple density profile (A2), we calculate the mass coordinate M_r , free-fall time t_{ff} , and their derivatives as follows,

$$M_r = M_{\text{core}} + 3M_{\text{core}} \ln\left(\frac{r}{R_{\text{core}}}\right) \quad (R_{\text{core}} < r), \quad (\text{A3})$$

$$\frac{dM_r}{dr} = \frac{3M_{\text{core}}}{r}, \quad (\text{A4})$$

$$\frac{dt_{\text{ff}}}{dr} = \frac{3}{2} \left(\frac{\pi^2}{8G}\right)^{1/2} \left(\frac{r}{M_r}\right)^{1/2} \left[1 - \frac{M_{\text{core}}}{M_r}\right] \simeq \frac{3}{2} \left(\frac{\pi^2}{8G}\right)^{1/2} \left(\frac{r}{M_r}\right)^{1/2}. \quad (\text{A5})$$

Then, we obtain the mass accretion rate as

$$\dot{M} \simeq \frac{3M_{\text{core}}}{r} \frac{2}{3} \left(\frac{8G}{\pi^2}\right)^{1/2} \left(\frac{M_r}{r}\right)^{1/2} \simeq \frac{2M_{\text{core}}}{t}. \quad (\text{A6})$$

The jet injection time may depend on the detail of the jet-launching mechanism. However, we have showed that whenever the jet is launched from the central BH and accretion disk system, as long as the injection time is much shorter than the jet breakout time, the result does not change so much (Matsumoto et al. 2015). For simplicity, we consider the free-fall time of the stellar core as the jet injection time,

$$t_{\text{in}} = \sqrt{\frac{\pi^2 R_{\text{core}}^3}{8GM_{\text{core}}}} \simeq 9.7 \times 10^{-1} \text{ s} \left(\frac{\rho_{\text{core}}}{4.6 \times 10^6 \text{ g cm}^{-3}}\right)^{-1/2}. \quad (\text{A7})$$

The jet breakout time is estimated by $t_{\text{b}} \simeq R_*/\beta_{\text{h}}c$, where β_{h} is the jet head velocity divided by the speed of light c . From the conservation of the momentum and energy flux at the jet head, the velocity β_{h} is given by the jet luminosity and the stellar density as (Matzner 2003; Bromberg et al. 2011)

$$\begin{aligned} \beta_{\text{h}} &\simeq \left(\frac{L_j}{\rho(r_{\text{h}})c^3 \Sigma_{\text{h}}}\right)^{1/2} \simeq \left(\frac{8\eta_j}{3c\theta^2}\right)^{1/2} \left(\frac{r_{\text{h}}}{t}\right)^{1/2} \\ &\simeq \frac{8\eta_j}{3\theta^2} \simeq 2.2 \times 10^{-1} \left(\frac{\eta_j}{6.2 \times 10^{-4}}\right) \left(\frac{\theta}{5^\circ}\right)^{-2}. \end{aligned} \quad (\text{A8})$$

In the first line, the quantity $\Sigma_{\text{h}} = \pi(r_{\text{h}}\theta)^2$ means the cross section of the jet head. From the first line to the second line, we use the fact that the jet head position r_{h} is given by $r_{\text{h}} \simeq \beta_{\text{h}}ct$. As shown in Eq. (A8), the jet head velocity is constant in the density profile of $\rho \propto r^{-3}$ for a constant opening angle θ (Matsumoto et al. 2015). Then, we obtain the jet breakout time as

$$t_{\text{b}} \simeq \frac{3\theta^2 R_*}{8\eta_{\text{j}}c} \simeq 8.9 \times 10^3 \text{ s} \left(\frac{\eta_{\text{j}}}{6.2 \times 10^{-4}} \right)^{-1} \left(\frac{\theta}{5^\circ} \right)^2 \left(\frac{R_*}{5.8 \times 10^{13} \text{ cm}} \right). \quad (\text{A9})$$

Substituting Eqs. (A6), (A7) and (A9) into Eq. (A1), we get the formula for the cocoon energy,

$$\begin{aligned} E_{\text{c}} &= 2\eta_{\text{j}} M_{\text{core}} c^2 \ln \left(\frac{t_{\text{b}}}{t_{\text{in}}} \right) \\ &= 2.0 \times 10^{56} \text{ erg} \left(\frac{\eta_{\text{j}}}{6.2 \times 10^{-4}} \right) \left(\frac{M_{\text{core}}}{9.6 \times 10^3 M_{\odot}} \right) \ln \left[\left(\frac{t_{\text{b}}}{8.9 \times 10^3 \text{ s}} \right) \left(\frac{t_{\text{in}}}{9.7 \times 10^{-1} \text{ s}} \right)^{-1} \right]. \end{aligned} \quad (\text{A10})$$

This equation reproduces the cocoon energy shown in Table 1, which are obtained by numerically integrating Eq. (A1).

Next, we also estimate the cocoon mass M_{c} at the jet breakout. The cocoon mass M_{c} is defined as the mass in the cocoon when the jet head breaks out of the stellar surface. Then, the cocoon mass is equal to the stellar mass within the volume where the cocoon expands in the progenitor. We approximate the shape of the cocoon component as a cone whose height is the distance of the jet head from the stellar center, and whose radius is the distance of the cocoon surface from the jet axis. We evaluate the cocoon mass as follows,

$$M_{\text{c}} \simeq \frac{M_*}{4\pi R_*^3/3} \times \frac{1}{3} \pi R_{\text{c}}^2 R_*, \quad (\text{A11})$$

where R_{c} is the radius of the cocoon component at the jet breakout time. In the second factor in Eq. (A11), we use the fact that when the jet head breaks out of the progenitor, the height of the cocoon is equal to the stellar radius R_* .

The radius is given by $R_{\text{c}} \simeq \beta_{\text{c}}ct_{\text{b}}$, where β_{c} is the velocity of the cocoon component expanding in the progenitor star. The velocity is estimated by the cocoon pressure P_{c} and the mean density in the cocoon component $\bar{\rho}$ as (Begelman & Cioffi 1989)

$$\beta_{\text{c}} \simeq \sqrt{\frac{P_{\text{c}}}{\bar{\rho}c^2}}. \quad (\text{A12})$$

Assuming that the cocoon is radiation-pressure-dominated, the cocoon pressure is given by $P_{\text{c}} \simeq E_{\text{c}}/\pi r_{\text{h}}r_{\text{c}}^2$. The mean density of the cocoon component $\bar{\rho}$ is also approximated by $\bar{\rho} \simeq 3M_{\text{r}_{\text{h}}}/4\pi r_{\text{h}}^3$. Substituting the expression of the cocoon pressure and the mean density and Eqs. (A3) and (A10) into Eq. (A12), we obtain

$$\beta_{\text{c}} \simeq \left(\frac{8\eta_{\text{j}}}{3} \frac{\ln(t/t_{\text{in}})}{1 + 3 \ln(r_{\text{h}}/R_{\text{core}})} \right)^{1/2} \frac{\beta_{\text{h}}ct}{r_{\text{c}}}. \quad (\text{A13})$$

Using the fact that the second factor in the parenthesis in Eq.(A13) is of the order of 3.4×10^{-1} at the jet breakout and that the cocoon radius is given by $r_{\text{c}} \simeq \beta_{\text{c}}ct$, we obtain the cocoon velocity as

$$\beta_{\text{c}} \simeq \left(\frac{8\eta_{\text{j}}}{3} \frac{\ln(t_{\text{b}}/t_{\text{in}})}{1 + 3 \ln(R_*/R_{\text{core}})} \right)^{1/4} \beta_{\text{h}}^{1/2} \simeq 7.2 \times 10^{-2} \left(\frac{\eta_{\text{j}}}{6.2 \times 10^{-4}} \right)^{3/4} \left(\frac{\theta}{5^\circ} \right)^{-1}. \quad (\text{A14})$$

With Eq. (A14), Eq. (A11) gives

$$\begin{aligned} M_{\text{c}} &\simeq \frac{1}{4} M_* \left(\frac{\beta_{\text{c}}}{\beta_{\text{h}}} \right)^2 \\ &\simeq 2.8 \times 10^3 M_{\odot} \left(\frac{M_*}{10^5 M_{\odot}} \right) \left(\frac{\eta_{\text{j}}}{6.2 \times 10^{-4}} \right)^{-1/2} \left(\frac{\theta}{5^\circ} \right)^2. \end{aligned} \quad (\text{A15})$$

This roughly reproduces the numerical results in Table 1.

B. LIGHT CURVE MODEL

We describe one-zone analytical formulae for the light curves of cocoon emission based on Arnett (1980); Popov (1993); Nakauchi et al. (2013); Dexter & Kasen (2013). We consider an expanding cocoon fireball which is non-relativistic and radiation-pressure-dominated. Immediately after the breakout, the cocoon fireball is accelerated by the pressure PdV work. When its radius gets about doubled, we can assume that the cocoon energy is equally divided into the kinetic and the internal energy, $E_{\text{kin}} \sim E_{\text{int}} \sim E_{\text{c}}/2$, and that the cocoon fireball starts homologous expansion

$v \propto r$. For simplicity, we also assume that the cocoon fireball is homogeneous. In this phase, we can calculate light curves of the cocoon emission in the same way as Type IIP SNe, only with the progenitor's radius R_* , the cocoon energy E_c , and mass M_c at the jet breakout. Since the cocoon fireball expands with a constant velocity, the cocoon radius is given by

$$R_c(t) = v_c t + R_c(0), \quad (\text{B1})$$

where $R_c(0) = 2R_*$ and v_c is the cocoon velocity which is evaluated by $v_c \sim \sqrt{5E_c/3M_c}$, where the numerical factor arises from the calculation of the total kinetic energy of the cocoon fireball ($E_{\text{kin}} \simeq \int (\rho v^2/2) 4\pi r^2 dr = 3M_c v_c^2/10$). We should note that we set the origin of time at the moment when the cocoon fireball begins to expand homologously.

We calculate the thermal evolution of the cocoon fireball with the first law of thermodynamics,

$$\frac{dE_{\text{int}}}{dt} = -P \frac{dV}{dt} + H - L, \quad (\text{B2})$$

where E_{int} , P , $V = 4\pi R_c^3/3$, H , and L are the total internal energy of the cocoon fireball, the cocoon pressure, the cocoon volume, the heating rate from the external energy source, and the radiative cooling rate, respectively. In our study, we ignore the heating source of the cocoon fireball. Since the cocoon fireball is radiation-pressure-dominated, the cocoon pressure P is given by $P = E_{\text{int}}/3V$.

First, we ignore the effect of hydrogen recombination on the opacity. As long as the effective temperature of the cocoon fireball T_{eff} is higher than the recombination temperature $T_{\text{ion}} \simeq 6000$ K, we assume that the cocoon fireball is fully ionized. Then, the cocoon fireball is optically thick and its luminosity is given by the diffusion approximation as,

$$\begin{aligned} L &\simeq 4\pi R_c^2 \frac{cV}{3\kappa M_c} \frac{E_{\text{int}}}{V R_c} = \frac{4\pi c R_c}{3\kappa M_c} E_{\text{int}} \\ &= \frac{t + t_e}{t_d^2} E_{\text{int}}, \end{aligned} \quad (\text{B3})$$

where κ is the cocoon opacity. In Eq. (B3), we define the expansion time t_e and the diffusion time t_d as follows,

$$t_e := \frac{R_c(0)}{v_c} \simeq 1.1 \times 10^4 \text{ s } R_{c,14} E_{c,56}^{-1/2} M_{c,3}^{1/2}, \quad (\text{B4})$$

$$t_d := \sqrt{\frac{3\kappa M_c}{4\pi v_c c}} \simeq 2.5 \times 10^7 \text{ s } E_{c,56}^{-1/4} M_{c,3}^{3/4}, \quad (\text{B5})$$

where $R_{c,14} = R_c(0)/10^{14}$ cm, $E_{c,56} = E_c/10^{56}$ erg, and $M_{c,3} = M_c/10^3 M_\odot$. In the second equality of Eq. (B5), we substitute the opacity value for $\kappa = 0.35 \text{ cm}^2 \text{ g}^{-1}$, which is the Thomson scattering opacity of the primordial chemical composition. Using Eqs. (B1), (B2), and (B3), we obtain a differential equation for the cocoon luminosity,

$$\frac{dL}{dt} + \frac{t + t_e}{t_d^2} L = 0. \quad (\text{B6})$$

Integration of Eq. (B6) yields the time evolution of the luminosity,

$$L(t) = \frac{t_e E_c}{2t_d^2} \exp\left(-\frac{1}{2t_d^2}(t^2 + 2t_e t)\right) \simeq 9.0 \times 10^{44} \text{ erg s}^{-1} R_{c,14} E_{c,56} M_{c,3}^{-1} \exp\left(-\frac{1}{2t_d^2}(t^2 + 2t_e t)\right). \quad (\text{B7})$$

When the exponential factor of this equation is almost unity during this phase ($t_i^2/2t_d^2 \lesssim 1$, see below), the bolometric luminosity does not change so much. We equate Eq. (B7) with $L = 4\pi R_c(t)^2 \sigma_{\text{SB}} T_{\text{eff}}(t)^4$, where σ_{SB} is the Stefan-Boltzmann constant, and get the time evolution of the effective temperature as

$$T_{\text{eff}}(t) \simeq \left(\frac{cR_c(0)}{10\kappa\sigma_{\text{SB}}(t + t_e)^2}\right)^{1/4} \exp\left(-\frac{1}{8t_d^2}(t^2 + 2t_e t)\right). \quad (\text{B8})$$

In this phase, the photospheric velocity v_{ph} is roughly evaluated by the cocoon velocity v_c . Then using the definition of the cocoon velocity, we obtain

$$v_{\text{ph}} \sim \left(\frac{5E_c}{3M_c}\right)^{1/2} \simeq 3.0 \times 10^{-1} c E_{c,56}^{1/2} M_{c,3}^{-1/2}. \quad (\text{B9})$$

Next, we take the recombination effect into account. When the effective temperature gets smaller than the critical value, a recombination wave starts to recede into the center. We define the time t_i as the moment when the effective temperature drops to the critical one $T_{\text{eff}}(t_i) = T_{\text{ion}}$. Then, the time t_i is given by

$$t_i \simeq \left(\frac{cR_c(0)}{10\kappa\sigma_{\text{SB}}}\right)^{1/2} T_{\text{ion}}^{-2} \simeq 3.4 \times 10^6 \text{ s } R_{c,14}^{1/2}, \quad (\text{B10})$$

where we assume that $t_i \gg t_e$ and the exponential factor in Eq. (B8) is unity. These assumptions are justified for the cocoon parameters we consider ($t_e/t_i \ll 1$ and $t_i^2/8t_d^2 \ll 1$). Since it is transparent outside of the recombination wave, we identify the photospheric radius $R_{\text{ph}}(t) := x_i(t)R_c(t)$ as the recombination front, where the temperature is equal to the recombination temperature. We also consider the thermal evolution of the cocoon fireball with Eq. (B2) only for the volume within the photospheric radius. Then, the internal energy within the photospheric radius is given by $\tilde{E}_{\text{int}} = E_{\text{int}}\tilde{V}/V$, where $\tilde{V} := x_i(t)^3V$ is the volume within the photospheric radius. The luminosity is given by $L = 4\pi R_{\text{ph}}(t)^2\sigma_{\text{SB}}T_{\text{ion}}^4$. The diffusion approximation also gives the luminosity as

$$L \simeq 4\pi x_i(t)^2 R_c(t)^2 \frac{Vc}{3\kappa M_c} \frac{\tilde{E}_{\text{int}}}{\tilde{V}x_i(t)R_c(t)} = \frac{4\pi c}{3\kappa M_c} \frac{R_c(t)}{x_i(t)^2} \tilde{E}_{\text{int}}. \quad (\text{B11})$$

Equating these expressions, we obtain the internal energy within the photospheric radius as

$$\tilde{E}_{\text{int}} = \frac{3\kappa M_c \sigma_{\text{SB}} T_{\text{ion}}^4}{c} R_c(t) x_i(t)^4. \quad (\text{B12})$$

With Eqs. (B11) and (B12), the first law of thermodynamics yields a differential equation for $x_i(t)$ as

$$\frac{dx_i}{dt} = -\frac{2x_i}{5t} - \frac{t}{5t_d^2 x_i}, \quad (\text{B13})$$

where we approximate the cocoon radius as $R_c(t) \sim v_c t$ ($t > t_i \gg t_e$). We integrate Eq. (B13) with the initial condition $x_i(t_i) = 1$, and obtain the time evolution of the photospheric radius

$$R_{\text{ph}}(t)^2 = x_i(t)^2 R_c(t)^2 = v_c^2 \left[t^{6/5} t_i^{4/5} \left(1 + \frac{t_i^2}{7t_d^2} \right) - \frac{t^4}{7t_d^2} \right] \quad (t > t_i). \quad (\text{B14})$$

We summarize the time evolutions of the bolometric luminosity, the effective temperature, and the photospheric radius as,

$$L(t) = \begin{cases} \frac{t_e E_c}{2t_d^2} \exp\left(-\frac{t^2}{2t_d^2}\right) & (t_e \ll t < t_i) \\ 4\pi\sigma_{\text{SB}}T_{\text{ion}}^4 v_c^2 \left[t^{6/5} t_i^{4/5} \left(1 + \frac{t_i^2}{7t_d^2} \right) - \frac{t^4}{7t_d^2} \right] & (t > t_i), \end{cases} \quad (\text{B15})$$

$$T_{\text{eff}}(t) = \begin{cases} \left(\frac{cR(0)}{10\kappa\sigma_{\text{SB}}} \right)^{1/4} t^{-1/2} \exp\left(-\frac{t^2}{8t_d^2}\right) & (t_e \ll t < t_i) \\ T_{\text{ion}} & (t > t_i), \end{cases} \quad (\text{B16})$$

$$R_{\text{ph}}(t) = \begin{cases} v_c t & (t_e \ll t < t_i) \\ v_c \left[t^{6/5} t_i^{4/5} \left(1 + \frac{t_i^2}{7t_d^2} \right) - \frac{t^4}{7t_d^2} \right]^{1/2} & (t > t_i). \end{cases} \quad (\text{B17})$$

The duration of the cocoon emission is given by solving $L(\Delta t_{\text{co}}) = 0$. We obtain the duration as

$$\Delta t_{\text{co}} = 7^{5/14} t_i^{2/7} t_d^{5/7} \simeq 2.8 \times 10^7 \text{ s } R_{c,14}^{1/7} E_{c,56}^{-5/28} M_{c,3}^{15/28}. \quad (\text{B18})$$

The time $t_{2\text{nd}}$ when the light curves show the second peak is also given by solving $dL/dt = 0$. We get the time as

$$t_{2\text{nd}} = \left(\frac{21}{10} \right)^{5/14} t_i^{2/7} t_d^{5/7} \simeq 1.9 \times 10^7 \text{ s } R_{c,14}^{1/7} E_{c,56}^{-5/28} M_{c,3}^{15/28}. \quad (\text{B19})$$

Then, the bolometric luminosity reaches

$$L_{2\text{nd}} = 4\pi\sigma_{\text{SB}}T_{\text{ion}}^4 v_c^2 \left[t_{\text{max}t_i}^{6/5} t_i^{4/5} \left(1 + \frac{t_i^2}{7t_d^2} \right) - \frac{t_{\text{max}}^4}{7t_d^2} \right] \simeq 4.7 \times 10^{45} \text{ erg s}^{-1} R_{c,14}^{4/7} E_{c,56}^{11/14} M_{c,3}^{-5/14}. \quad (\text{B20})$$

The photospheric velocity at this moment is expressed by

$$v_{\text{ph}}(t_{2\text{nd}}) = x_i(t_{2\text{nd}})v_c \simeq 3.5 \times 10^9 \text{ cm s}^{-1} R_{c,14}^{1/7} E_{c,56}^{4/7} M_{c,3}^{-5/7}. \quad (\text{B21})$$

The observed flux of the cocoon emission is given by

$$F_{\lambda_{\text{obs}}}(t_{\text{obs}})d\lambda_{\text{obs}} = \pi B_{\lambda}(T_{\text{eff}}(t)) \frac{R_{\text{ph}}(t)^2}{d_L^2} d\lambda, \quad (\text{B22})$$

where $B_\lambda(T) = 2hc^2/\lambda^5(\exp(hc/\lambda k_B T) - 1)^{-1}$ and d_L are the Planck function and the luminosity distance, respectively. The time in the observer frame t_{obs} and the observed wavelength λ_{obs} are related with the time and the wavelength in the progenitor rest frame as $t_{\text{obs}} = (1+z)t$ and $\lambda_{\text{obs}} = (1+z)\lambda$.

REFERENCES

- Abel, T., Bryan, G. L., & Norman, M. L. 2002, *Science*, 295, 93
 Agarwal, B., & Khochfar, S. 2015, *MNRAS*, 446, 160
 Agarwal, B., Khochfar, S., Johnson, J. L., et al. 2012, *MNRAS*, 425, 2854
 Agarwal, B., Smith, B., Glover, S., Natarajan, P., & Khochfar, S. 2015, arXiv:1504.04042
 Alexander, T., & Natarajan, P. 2014, *Science*, 345, 1330
 Alvarez, M. A., Wise, J. H., & Abel, T. 2009, *ApJ*, 701, L133
 Arnett, W. D. 1980, *ApJ*, 237, 541
 Aykotalp, A., Wise, J. H., Spaans, M., & Meijerink, R. 2014, *ApJ*, 797, 139
 Barthelmy, S. D., Barbier, L. M., Cummings, J. R., et al. 2005, *Space Sci. Rev.*, 120, 143
 Becerra, F., Greif, T. H., Springel, V., & Hernquist, L. E. 2015, *MNRAS*, 446, 2380
 Begelman, M. C., & Cioffi, D. F. 1989, *ApJ*, 345, L21
 Blandford, R. D., & Znajek, R. L. 1977, *MNRAS*, 179, 433
 Bose, S., Kumar, B., Sutaria, F., et al. 2013, *MNRAS*, 433, 1871
 Bradley, L. D., Trenti, M., Oesch, P. A., et al. 2012, *ApJ*, 760, 108
 Bromberg, O., Nakar, E., Piran, T., & Sari, R. 2011, *ApJ*, 740, 100
 Bromm, V., Coppi, P. S., & Larson, R. B. 1999, *ApJ*, 527, L5
 —. 2002, *ApJ*, 564, 23
 Bromm, V., & Loeb, A. 2003, *ApJ*, 596, 34
 Chandrasekhar, S. 1964, *ApJ*, 140, 417
 Chen, K.-J., Heger, A., Woosley, S., et al. 2014, *ApJ*, 790, 162
 de Souza, R. S., Yoshida, N., & Ioka, K. 2011, *A&A*, 533, A32
 Dexter, J., & Kasen, D. 2013, *ApJ*, 772, 30
 Dhungana, G., Kehoe, R., Vinko, J., et al. 2015, ArXiv e-prints, arXiv:1509.01721
 Dijkstra, M., Ferrara, A., & Mesinger, A. 2014, *MNRAS*, 442, 2036
 Dijkstra, M., Haiman, Z., Mesinger, A., & Wyithe, J. S. B. 2008, *MNRAS*, 391, 1961
 Fan, X. 2006, *New A Rev.*, 50, 665
 Fryer, C. L., & Heger, A. 2011, *Astronomische Nachrichten*, 332, 408
 Gal-Yam, A. 2012, *Science*, 337, 927
 Gardner, J. P., Mather, J. C., Clampin, M., et al. 2006, *Space Sci. Rev.*, 123, 485
 Gendre, B., Stratta, G., Atteia, J. L., et al. 2013, *ApJ*, 766, 30
 Gou, L. J., Mészáros, P., Abel, T., & Zhang, B. 2004, *ApJ*, 604, 508
 Gunn, J. E., & Peterson, B. A. 1965, *ApJ*, 142, 1633
 Hamuy, M. 2003, *ApJ*, 582, 905
 Hirano, S., Hosokawa, T., Yoshida, N., et al. 2014, *ApJ*, 781, 60
 Hosokawa, T., Hirano, S., Kuiper, R., et al. 2015, ArXiv e-prints, arXiv:1510.01407
 Hosokawa, T., Omukai, K., & Yorke, H. W. 2012, *ApJ*, 756, 93
 Hosokawa, T., Yorke, H. W., Inayoshi, K., Omukai, K., & Yoshida, N. 2013, *ApJ*, 778, 178
 Inayoshi, K., & Haiman, Z. 2014, *MNRAS*, 445, 1549
 Inayoshi, K., Haiman, Z., & Ostriker, J. P. 2015a, ArXiv e-prints, arXiv:1511.02116
 Inayoshi, K., & Omukai, K. 2012, *MNRAS*, 422, 2539
 Inayoshi, K., & Tanaka, T. L. 2015, *MNRAS*, 450, 4350
 Inayoshi, K., Visbal, E., & Kashiyama, K. 2015b, *MNRAS*, 453, 1692
 Johnson, J. L., Whalen, D. J., Agarwal, B., Paardekooper, J.-P., & Khochfar, S. 2014, *MNRAS*, 445, 686
 Johnson, J. L., Whalen, D. J., Even, W., et al. 2013, *ApJ*, 775, 107
 Kashiyama, K., Nakauchi, D., Suwa, Y., Yajima, H., & Nakamura, T. 2013, *ApJ*, 770, 8
 Komissarov, S. S., & Barkov, M. V. 2010, *MNRAS*, 402, L25
 Lamb, D. Q., & Reichart, D. E. 2000, *ApJ*, 536, 1
 Latif, M. A., Schleicher, D. R. G., Schmidt, W., & Niemeyer, J. 2013, *MNRAS*, 433, 1607
 Laureijs, R., Amiaux, J., Arduini, S., et al. 2011, ArXiv e-prints, arXiv:1110.3193
 Levan, A. J., Tanvir, N. R., Starling, R. L. C., et al. 2014, *ApJ*, 781, 13
 Litvinova, I. Y., & Nadezhin, D. K. 1985, *Soviet Astronomy Letters*, 11, 145
 MacFadyen, A. L., & Woosley, S. E. 1999, *ApJ*, 524, 262
 Madau, P., Haardt, F., & Dotti, M. 2014, *ApJ*, 784, L38
 Matsumoto, T., Nakauchi, D., Ioka, K., Heger, A., & Nakamura, T. 2015, *ApJ*, 810, 64
 Matzner, C. D. 2003, *MNRAS*, 345, 575
 Matzner, C. D., & McKee, C. F. 1999, *ApJ*, 510, 379
 Mesinger, A., Johnson, B. D., & Haiman, Z. 2006, *ApJ*, 637, 80
 Mesler, R. A., Whalen, D. J., Smidt, J., et al. 2014, *ApJ*, 787, 91
 Mészáros, P., & Rees, M. J. 2010, *ApJ*, 715, 967
 Milosavljević, M., Bromm, V., Couch, S. M., & Oh, S. P. 2009, *ApJ*, 698, 766
 Mortlock, D. J., Warren, S. J., Venemans, B. P., et al. 2011, *Nature*, 474, 616
 Nagakura, H., Suwa, Y., & Ioka, K. 2012, *ApJ*, 754, 85
 Nakauchi, D., Kashiyama, K., Suwa, Y., & Nakamura, T. 2013, *ApJ*, 778, 67
 Nakauchi, D., Suwa, Y., Sakamoto, T., Kashiyama, K., & Nakamura, T. 2012, *ApJ*, 759, 128
 Omukai, K. 2001, *ApJ*, 546, 635
 Park, K., & Ricotti, M. 2011, *ApJ*, 739, 2
 Park, K., & Ricotti, M. 2012, *ApJ*, 747, 9
 Park, K., & Ricotti, M. 2013, *ApJ*, 767, 163
 Planck Collaboration, Ade, P. A. R., Aghanim, N., et al. 2015, ArXiv e-prints, arXiv:1502.01589
 Popham, R., Woosley, S. E., & Fryer, C. 1999, *ApJ*, 518, 356
 Popov, D. V. 1993, *ApJ*, 414, 712
 Regan, J. A., & Haehnelt, M. G. 2009, *MNRAS*, 396, 343
 Regan, J. A., & Haehnelt, M. G. 2009, *MNRAS*, 393, 858
 Regan, J. A., Johansson, P. H., & Haehnelt, M. G. 2014, *MNRAS*, 439, 1160
 Sakurai, Y., Hosokawa, T., Yoshida, N., & Yorke, H. W. 2015, *MNRAS*, 452, 755
 Schauer, A. T. P., Whalen, D. J., Glover, S. C. O., & Klessen, R. S. 2015, *MNRAS*, 454, 2441
 Schleicher, D. R. G., Palla, F., Ferrara, A., Galli, D., & Latif, M. 2013, *A&A*, 558, A59
 Shang, C., Bryan, G. L., & Haiman, Z. 2010, *MNRAS*, 402, 1249
 Spergel, D., Gehrels, N., Breckinridge, J., et al. 2013, arXiv:1305.5422

- Sugimura, K., Omukai, K., & Inoue, A. K. 2014, MNRAS, 445, 544
Susa, H., Hasegawa, K., & Tominaga, N. 2014, ApJ, 792, 32
Suwa, Y., & Ioka, K. 2011, ApJ, 726, 107
Tanaka, M., Moriya, T. J., & Yoshida, N. 2013, MNRAS, 435, 2483
Volonteri, M., & Rees, M. J. 2005, ApJ, 633, 624
Wanderman, D., & Piran, T. 2010, MNRAS, 406, 1944
Wang, F. Y., Bromm, V., Greif, T. H., et al. 2012, ApJ, 760, 27
Whalen, D. J., Johnson, J. L., Smidt, J., et al. 2013a, ApJ, 777, 99
Whalen, D. J., Even, W., Smidt, J., et al. 2013b, ApJ, 778, 17
Wise, J. H., Turk, M. J., & Abel, T. 2008, ApJ, 682, 745-757
Wolcott-Green, J., Haiman, Z., & Bryan, G. L. 2011, MNRAS, 418, 838
Woosley, S. E. 1993, ApJ, 405, 273
Woosley, S. E., & Heger, A. 2006, ApJ, 637, 914
Wu, X.-B., Wang, F., Fan, X., et al. 2015, Nature, 518, 512
Yoon, S.-C., & Langer, N. 2005, A&A, 443, 643
Yoshida, N., Abel, T., Hernquist, L., & Sugiyama, N. 2003, ApJ, 592, 645
Yoshida, N., Omukai, K., & Hernquist, L. 2008, Science, 321, 669
Yoshida, N., Omukai, K., Hernquist, L., & Abel, T. 2006, ApJ, 652, 6
Yue, B., Ferrara, A., Salvaterra, R., Xu, Y., & Chen, X. 2014, MNRAS, 440, 1263
Zalamea, I., & Beloborodov, A. M. 2011, MNRAS, 410, 2302